

Rapid 3D chemical-specific imaging of minerals using stimulated Raman scattering microscopy

Marie-Andrée Houle,^{a,b} Robert C. Burruss,^c Andrew Ridsdale,^b Douglas J. Moffatt,^b François Légaré^a and Albert Stolow^{b,d,e,*}

Raman microscopy, which offers chemical-specific imaging, has important applications in geological sciences. Conventional Raman imaging, however, is challenged by long acquisition times and can be overwhelmed by sample fluorescence. Here, we present the first applications of stimulated Raman scattering (SRS) microscopy, a nonlinear optical Raman technique, to samples of mineralogical interest. Combined with second harmonic generation microscopy, SRS offers a multimodal tool for rapid imaging of mineral samples with chemical specificity, structural sensitivity, and excellent three-dimensional resolution. Our spectral focusing implementation allows for very rapid scanning of Raman spectral lineshapes, with an adjustable spectral resolution (set here to 25 cm^{-1}) and an overall tuning range of $400\text{--}4500\text{ cm}^{-1}$. In mineralogical applications, this wide-tuning range offers hyperspectral imaging of both trapped organics, via the CH region ($\sim 2900\text{ cm}^{-1}$), and the lower frequency ($< 1000\text{ cm}^{-1}$) 'fingerprint' modes important for mineral identification. The simultaneously acquired second harmonic generation image reveals details of the local crystallinity of non-centrosymmetric minerals such as quartz. As opposed to single-spectral-point imaging, we emphasize the importance of tuning over the Raman lineshape while imaging, to unambiguously distinguish the resonant Raman response from nonresonant background signals. Based on the range of samples studied here, we believe that multimodal SRS microscopy will become a valuable imaging tool in the earth sciences, particularly in mineralogy, petroleum, and mineral resources research. ©2017 Her Majesty the Queen in Right of Canada Journal of Raman Spectroscopy ©2017 John Wiley & Sons, Ltd.

Keywords: Raman; stimulated Raman scattering; Geology; mineralogy; second harmonic generation; nonlinear microscopy

Introduction

Three-dimensional imaging is widely applied in the earth sciences. The most common imaging method is X-ray computed tomography (CT), with more limited applications being magnetic resonance imaging and neutron CT.^[1] Advances in focused synchrotron X-ray sources have pushed voxel dimensions in microfocused X-ray CT imaging to sub-micrometer dimensions, providing unprecedented detail in studies of fossil structure, pore geometry, and mineral textures. Laser scanning confocal microscopy is being applied in geomicrobiology^[2] and paleobiology for 3D imaging of microbe-mineral interactions, biofilms, and fossils. Confocal Raman imaging, widely used for point analyses in geologic materials, is beginning to be used more frequently for 2D imaging of minerals and fossil organic matter. Unlike laser scanning confocal microscopy with fluorescence contrast, 2D Raman images contain vibrational spectral information at each pixel, providing the chemical-specific contrast needed for chemometric image analysis. Geoscience applications of Raman imaging are rapidly expanding in the studies of the oldest sedimentary rocks on Earth for evidence bearing on the origin of life^[3,4] and in studies of extraterrestrial materials and Earth materials that are possible analogs of the surface of Mars for evidence of biological processes.^[5,6] Broader application of Raman imaging, especially 3D Raman imaging, has been limited in large part by the length of time needed to acquire single 2D images, which can take 10 s of minutes to hours, and by the inapplicability of Raman imaging to fluorescent samples.

To move beyond the limitations of conventional Raman imaging, we have begun to explore applications of nonlinear coherent

Raman imaging to geologic materials.^[7] Coherent Raman scattering (CRS) microscopy is a molecule-specific, third-order nonlinear optical imaging method wherein the contrast is achieved via vibrational Raman resonances.^[8–11] This technique is based on the interaction of two laser beams, at the pump frequency ω_p and the Stokes frequency ω_s , with their frequency difference $\Delta\omega = \omega_p - \omega_s$ matching the resonant vibrational Raman frequency of a specific molecule within the sample. Because it is a stimulated process, the signals from CRS are orders of magnitude higher than spontaneous Raman microscopy.^[12,13] Coherent anti-Stokes Raman scattering (CARS) and stimulated Raman scattering (SRS) microscopy are among the most popular CRS techniques. The main difference between these two techniques is the way the Raman signal is detected. CARS microscopy is a homodyne technique that

* Correspondence to: Albert Stolow, Quantum Photonic Sensing and Security Program, Security and Disruptive Technologies, National Research Council, Ottawa, ON K1A 0R6, Canada.
E-mail: albert.stolow@nrc-cnrc.gc.ca

a *Énergie, Matériaux et Télécommunications, L'Institut national de la recherche scientifique, Varennes, QC3X 1S2, Canada*

b *Quantum Photonic Sensing and Security Program, Security and Disruptive Technologies, National Research Council, Ottawa, ON K1A 0R6, Canada*

c *United States Geological Survey, Reston, VA, 20192, USA*

d *Department of Chemistry, University of Ottawa, Ottawa, ON, K1N 6N5, Canada*

e *Department of Physics, University of Ottawa, Ottawa, ON, K1N 6N5, Canada*

detects the blue-shifted anti-Stokes signal ($\omega_{AS} = 2\omega_p - \omega_s$). On the other hand, SRS microscopy is a heterodyne technique that detects the transferred modulation of either the pump or the Stokes beam.^[14] To efficiently detect this modulation, one of the laser beams is typically modulated at MHz frequencies,^[15] while the transfer of modulation to the other beam is detected using a lock-in amplifier. The SRS signal can be measured either by the loss of the pump signal, termed stimulated Raman loss (SRL), or by the gain in the Stokes signal, termed stimulated Raman gain. The SRL process is illustrated in Fig. 1(b) and is considered in the following discussion. SRS microscopy has the advantage of being free of the nonresonant background present in CARS microscopy caused by four-wave mixing^[16] that can reduce the chemical detection sensitivity^[17] and cause coherent imaging artifacts^[18–20] as well as well-known coherent distortions in the Raman spectrum.^[21] However, SRS microscopy suffers from other sources of nonresonant background signals that can overwhelm small resonant SRS signals.^[22] In general, the nonresonant background signal in SRS microscopy can originate from multiple sources: two-photon absorption (TPA), excited state absorption (ESA), cross-phase modulation (XPM), and thermal lensing (TL). TPA can arise from the simultaneous absorption of one pump plus one Stokes photon and is seen as a loss by the detection system and, therefore, is detected as an SRL signal.^[23] ESA is similar to TPA but involves a real intermediate state.^[24] In ESA, one photon from the Stokes beam is absorbed, exciting the molecule and increasing the absorptivity of the pump beam that can excite the molecule to a higher state. In contrast, TL and XPM arise from the refractive index change induced by the pump beam, as experienced by the Stokes beam. These transient refractive index changes modify the propagation of the transmitted Stokes beam to the detector and, hence, can appear as a modulated signal, depending on details of the collection optics. XPM is a purely instantaneous third-order nonlinear effect,^[25] whereas TL is caused by a time-averaged multiple pulse response that results from a temperature-induced variation of the refractive

index because of weak absorption of either the pump or the Stokes beam.^[26] TPA and ESA can be reduced by using longer wavelengths,^[27] whereas TL and XPM can be reduced by using collection optics with a large numerical aperture^[27] or by adopting a polarization–modulation configuration for the modulated beam.^[28]

Coherent Raman scattering microscopy was developed for use in biology and medicine.^[10,29–31] Much of this imaging was in the CH stretch region because of the importance of lipids in biological samples and the generally high signals that they produce. Only more recently has interest in the technique evolved to allow imaging of samples in the Raman fingerprint region ($1000\text{--}2000\text{ cm}^{-1}$).^[32–37] Important Raman resonances in minerals are usually at even lower frequencies ($<1000\text{ cm}^{-1}$). CRS microscopy of geologic samples, using CARS, was recently demonstrated.^[38] That study demonstrated rapid, multimodal chemical-specific 3D imaging of trapped fluid inclusions containing N_2 (2330 cm^{-1}), methane and crude oil (CH, $\sim 2900\text{ cm}^{-1}$), and water (OH, 3600 cm^{-1}).

Stimulated Raman scattering microscopy has other advantages over traditional Raman microscopy. SRS signals can be acquired simultaneously with second-order nonlinear processes such as second harmonic generation (SHG) and two-photon excitation fluorescence, allowing for multimodal imaging. Furthermore, due to the nonlinear interaction, the signal is inherently confocal, being generated only at the focus of the laser beams, allowing for 3D imaging. Importantly, SRS is relatively unaffected by sample fluorescence, a major impediment in traditional Raman microscopy.

Conventional Raman and SRS microscopy are each based on ‘chemical’ contrast due to Raman resonances. SRS microscopy can rapidly produce images, having a pixel dwell time on the order of 10 s of microseconds. In contrast, conventional Raman microscopy may typically have pixel dwell times on the order of 10 s of milliseconds, three orders of magnitude longer.^[39] Furthermore, SRS microscopy has excellent 3D imaging capabilities, with a depth resolution on the order of a micron^[15] and the potential to image deep into the sample (100 s of microns), depending

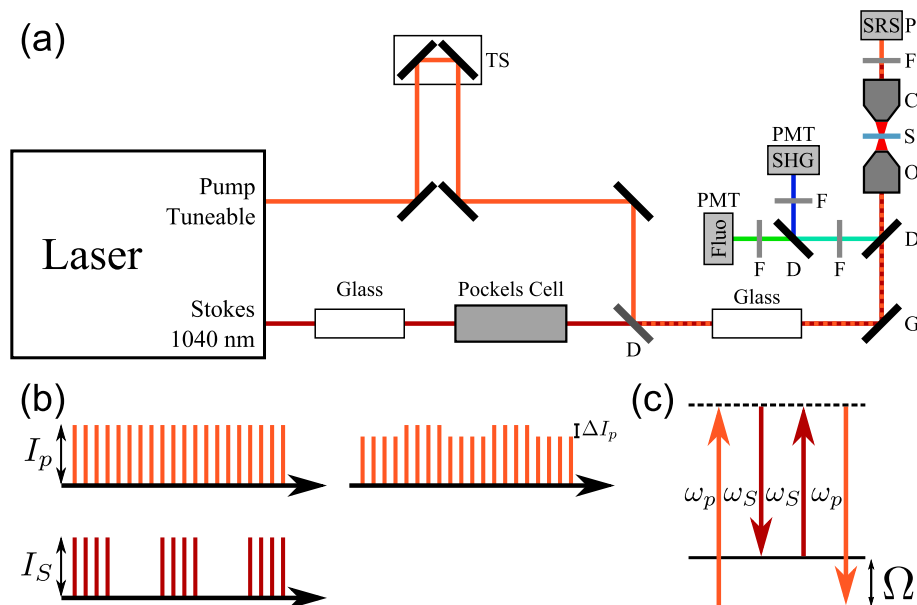


Figure 1. (a) Experimental setup for stimulated Raman scattering (SRS) microscopy: (TS) translation stage, (D) dichroic mirror, (G) galvanometer mirrors, (S) sample, (O) microscope objective, (C) condenser, (P) photodiode, (F) filters, and (PMT) photomultiplier tube. (b) Stimulated Raman loss scheme used in the present experiment where the Stokes beam intensity is modulated and, when a Raman mode is excited, the modulation intensity is transferred to the pump beam. (c) Energy diagram of the SRS process. [Colour figure can be viewed at wileyonlinelibrary.com]

on sample transparency/scattering and the working distance of the microscope objective. Finally, in contrast with conventional Raman microscopy, SRS microscopy is not affected by sample fluorescence as the detected signal has the same wavelength as the pump or Stokes laser, typically in the near infrared. On the other hand, SRS microscopy is currently more complex in its implementation, requiring two synchronized short pulse laser beams and attention to sources of electronic noise. As noted earlier, SRS can suffer from nonresonant background signals that can reduce the detection sensitivity and be falsely identified as resonant SRS signals. As we emphasize here, rapid scanning of the SRS spectrum is essential to confirm the true chemical identity of the species in question.

Here, we present the first applications of SRS microscopy in the field of mineralogy. We demonstrate rapid 3D multimodal imaging at Raman shifts ranging from 400 to 3700 cm^{-1} , making possible the bond-specific imaging of minerals at low Raman frequency as well as trapped organic matter in the fingerprint region and in the CH stretch region ($\sim 3000 \text{ cm}^{-1}$). In the following, we describe our experimental approach and then present results of multimodal SRS microscopy on specific rock samples that illustrate the advantages of this approach for the field of mineralogy.

Methods

Experimental setup

The experiments were performed using the chirped pulse (spectral focusing) arrangement shown in Fig. 1(a). A detailed account of our spectral focusing technique can be found in the work of Pegoraro *et al.*^[40] Briefly, both pump and Stokes pulses are linearly chirped. By changing the time delay between them, the instantaneous Raman frequency is varied, allowing users to select a specific frequency or to rapidly acquire a continuous scan, yielding the Raman spectrum over a specified frequency range. This arrangement may be used for either stimulated Raman gain in the Stokes beam or SRL in the pump beam. A femtosecond laser system (InSight DS+, Spectra-Physics, USA) produced both pump and Stokes beams. The Stokes beam was the fixed output with a central wavelength of 1040 nm and a transform-limited pulse duration of 180 fs (here chirped to ~ 1.1 ps). The pump beam was tunable over the range 680–1300 nm. The spectral bandwidth of the pump beam corresponded to a transform limited pulse duration of approximately 150 fs (here chirped to ~ 1.4 ps). Typically, the pump

wavelength was tuned from 790 to 992 nm, corresponding to a Raman-tuning range of 465–3040 cm^{-1} . In the present implementation, we chose to modulate the fixed 1040 nm output (for technical simplicity) and monitored the pump beam in an SRL configuration. A Pockels cell (350–160, Conoptics, USA) induced a square wave amplitude modulation of the Stokes beam at a frequency of 1.4 MHz. The pump and Stokes beams were combined using a dichroic mirror (1040dmbp, Chroma, USA). A fixed optical path length of glass, 60 and 85 cm of SF11 glass, was added to the pump and Stokes beam paths, respectively, inducing a positive chirp. This permitted rapid tuning of the Raman frequency by time-scanned spectral focusing.^[32] The time delay between the pump and the Stokes beam was controlled by a translation stage in the pump beam path.

The pump and Stokes beams were sent into an inverted microscope (IX-71, Olympus, Japan) and focused into the sample with a microscope objective (UPlanSapo, 20x, NA 0.75, Olympus, Japan). Galvanometer mirrors at the entrance of the microscope raster scanned the sample, providing an image. The pump beam was collected in the forward direction by a microscope objective (LUMPlanFI/IR, 40x, NA 0.8w, Olympus, Japan) and sent into a photodiode (FDS10X10, Thorlabs, USA) after being filtered by two different optical filters (BrightLine 850/310, Semrock, USA and 1064–71 NF, Iridian, Canada). In the backward direction, a dichroic mirror (720DCXXR, Chroma, USA) directed both back-reflected SHG and fluorescence signals through a shortpass filter (750SP, Chroma, USA). These were separated with a dichroic mirror (540 DCRX, Chroma, USA), and each detected by a photomultiplier tube after passing through a filter (520/10, Chroma, USA for the SHG channel, HQ630/140 for the fluorescence channel). The detected SHG signal was almost entirely composed of forward directed SHG signal that was backreflected into the photomultiplier tube by optical surfaces present in the forward direction. A function generator (DS345, Stanford Research Systems, USA) produced the modulation signal for the Pockels cell. The modulation reference signal was sent into a lock-in amplifier (UHFLI, Zurich Instruments). The photodiode signal was amplified by a transimpedance amplifier (DHPCA-100, Femto Messtechnik GmbH, Germany) that provided the signal input to the lock-in amplifier. The lock-in amplifier then extracted the SRS signal at the function generator frequency. A time constant of 20 μs was used, and the relative phase of the lock-in amplifier was adjusted to maximize the SRS signal.

The spectral scans shown here were obtained by acquiring images while continuously scanning the time delay between the

Table 1. : Experimental parameters

| Figure number | 2 and 3 | 4 | 5 | 6 | 7 |
|---|---------------------------|-----------------------------|----------------------------|----------------------------|----------------------------|
| Sample | WPA | Powder | M-K5A | B-1 | B-2 |
| Pump/Stokes power (mW) | 30/60 | 40/80 | 50/100 | 30/60 | 20/40 |
| Scan size (μm) | $112 \times 12 \times 70$ | $298 \times 298 \times 100$ | $298 \times 298 \times 50$ | $224 \times 224 \times 30$ | $298 \times 298 \times 50$ |
| Resolution (pixels) | 512×512 | 512×512 | 256×256 | 512×512 | 512×512 |
| Depth step for each pixel (μm) | 0.5 | | | | |
| Integration time ($\mu\text{s}/\text{pixel}$) | 16 | 16 | 31 | 16 | 16 |
| Objective | 20X, 0.75NA | | | | |
| Raman peak (cm^{-1}) | 465/2917 | 465/1088 | 465 | 1088 | 1088/1017 |
| Pump wavelength (nm) | 992/798 | 992/934 | 992 | 934 | 937 |
| Images average | 3 | 2 | 3 | 3 | 3 |
| Total scan time per pump wavelength (min) | 28 | 27 | 10 | 12 | 20 |

chirped pump and Stokes pulses. One data point in the spectrum corresponds to the average intensity across a region of interest (ROI) in an image. By adjusting the chirp parameters of the pump and Stokes beams and the speed of the translation stage, the effective spectral resolution can be varied. In the present case, the scan speed corresponded to 1.1 cm^{-1} per acquisition (spectral data point). With the chirp parameters implemented here, the Raman spectral resolution was approximately 25 cm^{-1} . For hyperspectral scans, each image (256×256 pixels) took 2 s to acquire, and the total acquisition time for a hyperspectral scan ranged between 5 to 10 min, depending on the frequency range. The parameters used for 3D volume imaging are given in Table 1. The images were acquired using ScanImage software that also controlled the galvanometer mirror

parameters and the sample XYZ position.^[41] The images were processed using ImageJ/FIJI^[42] and the plug-in 3D viewer was used to create the 3D volume images.

Samples selection and preparation

With one exception, all the samples studied here are thin sections of rocks that were previously used for studies of economic accumulations of petroleum or metallic ore deposits. These samples, described subsequently, were chosen to demonstrate the capabilities of multimodal 3D hyperspectral imaging of geological samples using SRS microscopy. Sample WPA is quartz (SiO_2), containing fluid inclusions^[43] filled with methane-rich natural gas. This sample tests SRS imaging in both CH region and low-frequency range (Si-O

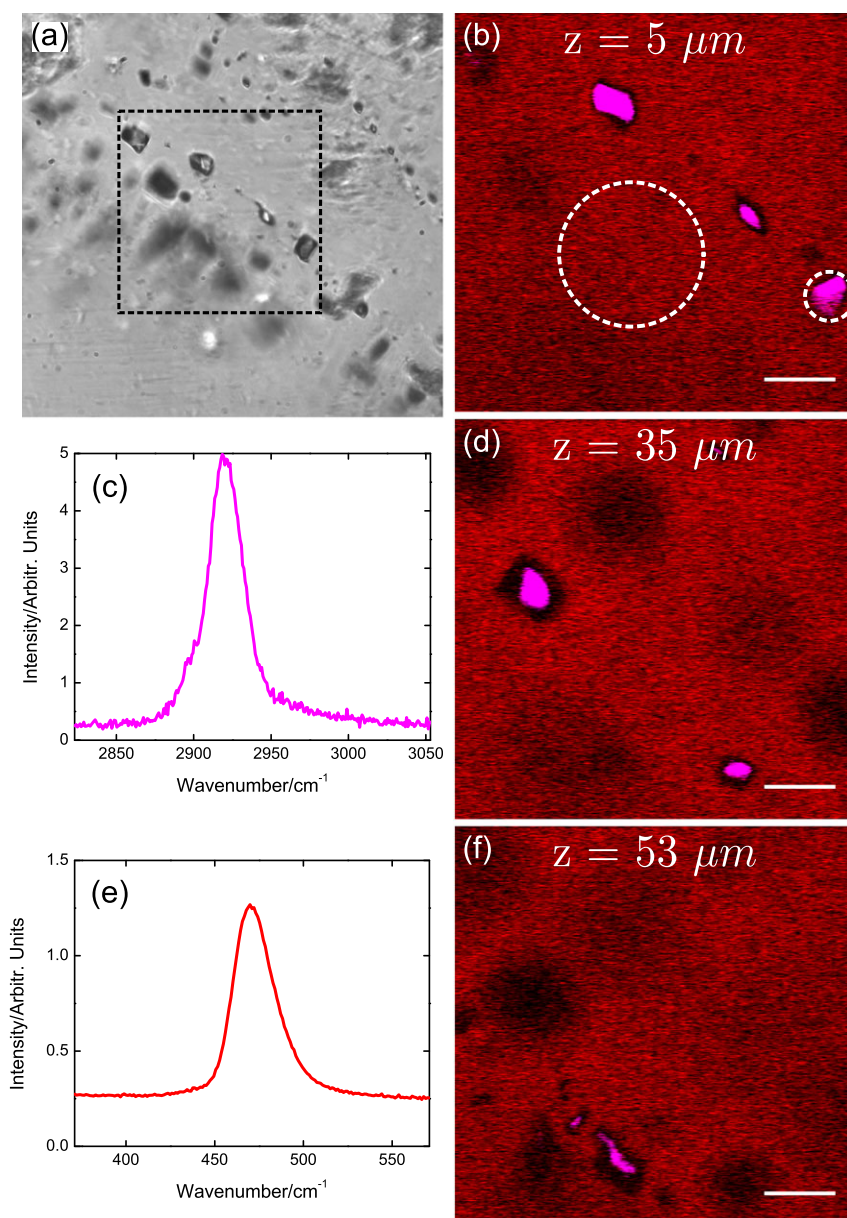


Figure 2. Sample WPA: (a) Bright-field transmitted-light image of a quartz sample containing methane-rich fluid inclusions. The square indicates the region imaged with stimulated Raman scattering (SRS) microscopy. (b), (d), and (f) SRS images of quartz (red) and methane fluid inclusions (magenta) at a depth of (b) 5, (d) 35, and (f) 53 μm from the surface of the sample. Panel (b) shows the region of interest used to measure the Raman spectrum for methane (c) and quartz (e). (c and e) SRS spectrum of (c) methane and (e) quartz acquired using the spectral focusing technique. The scale bars are 20 μm . [Colour figure can be viewed at wileyonlinelibrary.com]

bend, 464 cm^{-1}) of the fingerprint region. As an example of SRS chemically distinguishing two minerals, a sample of powdered quartz and calcite (CaCO_3), dispersed in cyanoacrylate cement, was prepared. The sample M-K5A contains large single crystals of quartz surrounded by microcrystalline quartz. This tests the multimodal (SRS and SHG) imaging capabilities of our SRS microscope, specifically using the SRS to chemically identify the mineral and SHG to simultaneously determine the nature of the local crystallinity. Samples B-1 and B-2 are mostly calcite, fine-grained sedimentary rock, with fossil foraminifera (B-1) or large single crystals which enclose small anhydrite (CaSO_4) crystals (B-2). These two samples test specific aspects of 3D SRS spectroscopic imaging such as 'chemical' contrast and nonresonant background effects.

All samples were prepared with standard petrographic thin section methods, either in university laboratories or by commercial service providers. The sections were doubly polished and mounted on glass slides with either epoxy or cyanoacrylate cement. The thickness of these sections ranged from 30 to approximately $100\ \mu\text{m}$.

Results and discussion

The multimodal imaging capabilities of our SRS microscopy method are demonstrated for geological imaging in Figs 2 and 3, here for the sample WPA. These figures present a sample of quartz

containing CH_4 -rich fluid inclusions, as shown by the conventional bright-field transmitted-light microscopy image in Fig. 2(a). Quartz has a sharp Raman peak at 464 cm^{-1} , while CH_4 has a strong Raman peak at 2917 cm^{-1} .^[44] By tuning the pump laser to 798 nm , we generated SRS signals from the CH_4 Raman bands. By tuning the pump laser to 992 nm , we probed the quartz (SiO_2 band) Raman band. This permitted chemical-specific imaging via each Raman band, yielding a composite image of the different molecules involved, as seen in Fig. 2(b) where the quartz is shown in red and the methane fluid inclusions are shown in magenta. Many fluid inclusions can be seen at different depths within the sample, as shown in Fig. 2(d) and (f). The SRS spectra are shown in Fig. 2(c) and (e), clearly showing the Raman vibrational bands of methane and quartz respectively confirming that the signals acquired were indeed from CH_4 and quartz. The ROI used to produce these Raman spectral scans are shown in Fig. 2(b).

One benefit of SRS as compared with that of conventional Raman microscopy is its relative speed of 3D imaging. In Fig. 3(a) and (b), we show a 3D volume ($112 \times 112 \times 68\ \mu\text{m}$) of the SRS signals from CH_4 -rich fluid inclusions (magenta) and quartz (red), showing the 3D locations of fluid inclusions within the sample. It is worth noting that Figs 2(b), (d), and (f); and 3(b) show the presence of darker regions having a weaker SRS signal 'behind' the methane fluid inclusions. This is caused by a slight modification of the beam divergence due to propagation through the fluid

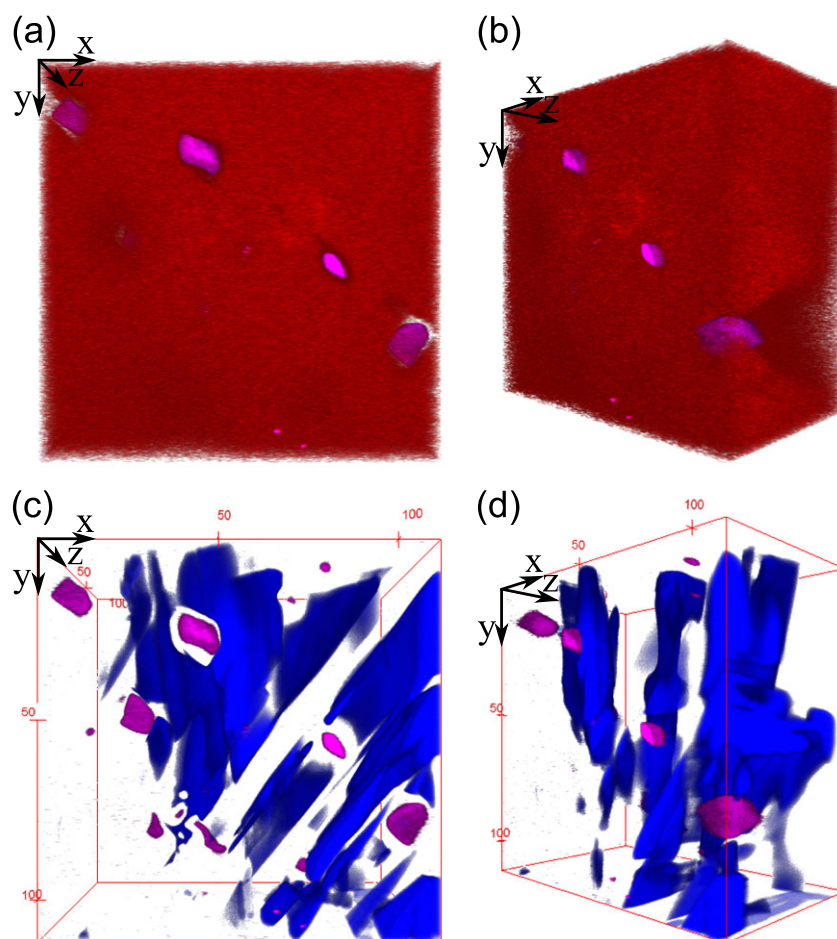


Figure 3. Sample WPA: (a) Front and (b) orthogonal view of a 3D volume of the stimulated Raman scattering signal from quartz (red) and fluid inclusion containing methane (magenta) from the samples shown in Fig. 2. (c) Front and (d) orthogonal view of a 3D volume of the second harmonic generation signal from quartz (blue) and fluid inclusions (magenta). [Colour figure can be viewed at wileyonlinelibrary.com]

inclusion, yielding a slightly smaller detected SRS signal. While the SRS signal may chemically identify the volume occupied by quartz, it does not give any additional information about its local structure. In Fig. 3(c) and (d), we show 3D volume images of SRS from CH₄-rich fluid inclusions (magenta) and the simultaneously acquired SHG signal from the quartz (blue). It can be seen that the spatial regions producing the SHG signal, generated by quartz, are very different from the SRS signal generated by quartz. Quartz is a non-centrosymmetric material, weakly allowing the generation of second harmonic signals. However, due to the Gouy phase shift, most of SHG signal is cancelled in a bulk uniform sample.^[45] Indeed, the Gouy phase shift causes the SHG signal generated in front of and behind the focal plane to be out of phase, cancelling each other by destructive interference. However, at an interface or at a twin plane, a break in symmetry occurs: the SHG generation along the focus is no longer cancelled, giving rise to a detectable SHG signal. SHG can therefore give information about the local crystal structure, such as the presence and orientation of twinning, which complements the information provided by SRS microscopy. Multimodal imaging using CARS microscopy was previously shown for methane fluid inclusions with SHG imaging of quartz.^[38] This is the first

time, to our knowledge, that SRS imaging of quartz samples has been performed simultaneously with SHG imaging.

We now consider the SRS imaging of a mixture of two minerals, quartz and calcite, as powders. Because of the nonlinear nature of SRS microscopy, the signal is only generated efficiently within the laser focal volume, allowing for inherently confocal high 3D-image resolution. In Fig. 4(a), we show a 3D volume image of quartz (red) and calcite (green) powders fixed in cyanoacrylate, with grain sizes ranging from a few microns to a few hundred microns. Calcite and quartz show sharp Raman peaks at 1088 and 466 cm⁻¹, respectively, as revealed by their SRS spectra in Fig. 4(b) and (c). In Fig. 4(d) and (e), we show a sub-region of the ROI, with two different angles of view, to demonstrate the 3D capability of the SRS technique. It is clear that small crystals of quartz and calcite, only a few micrometers in diameter, can be both spatially resolved and simultaneously chemically identified.

Multimodal SRS microscopy can be used to unveil different structures within a sub-volume of an ROI and provide information as to how it was formed. Using sample M-K5A, in Fig. 5, we show images of a quartz sample from a metallic ore deposit in which a relatively large single crystal of quartz was overgrown by microcrystalline

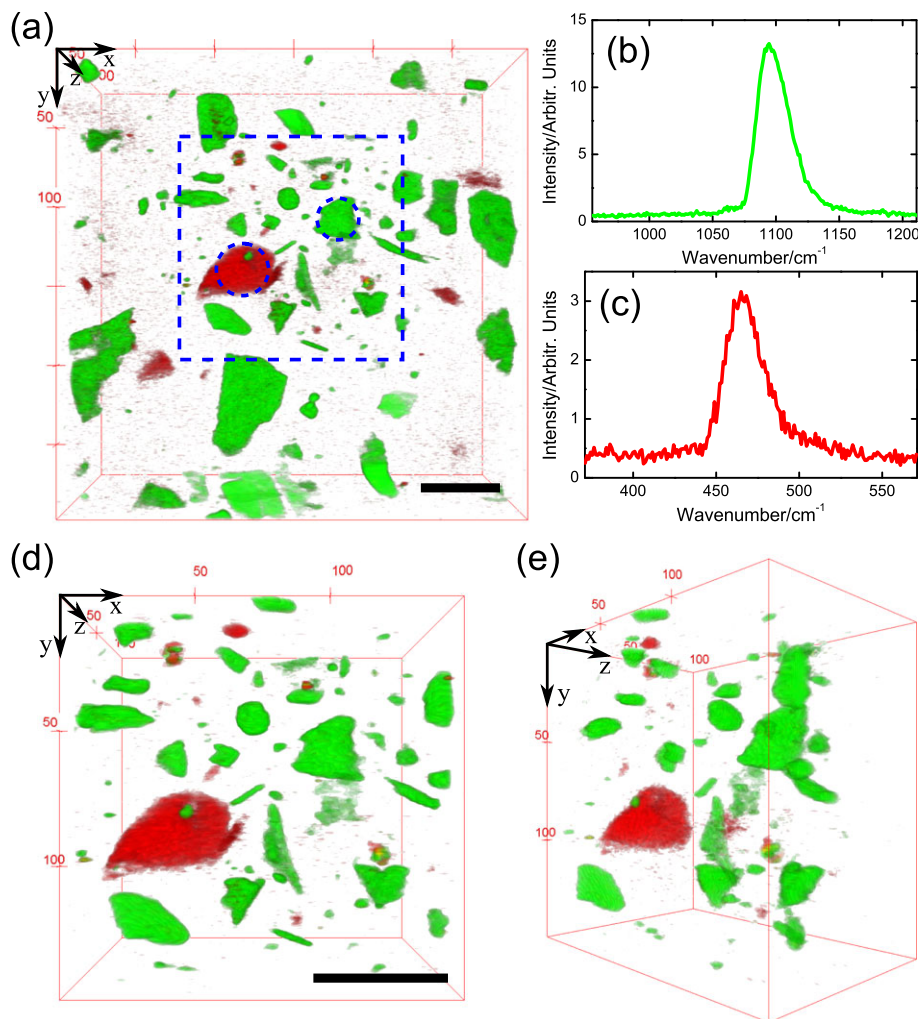


Figure 4. Powdered calcite and quartz: (a) stimulated Raman scattering (SRS) 3D volume image of calcite (green) and quartz (red) powder fixed in cyanoacrylate. The region of interest probed is $300 \times 300 \times 100 \mu\text{m}$. The blue square denotes the sub-region displayed in (d) and (e), and the circles denote the ROI used to create the SRS spectra in (b) and (c). (b) SRS spectrum of calcite. (c) SRS spectrum of quartz. (d) and (e) 3D volume image of calcite (green) and quartz (red) powder displayed in (d) front and (e) orthogonal view angles. The volume displayed is $150 \times 150 \times 100 \mu\text{m}$. Scale bars are $50 \mu\text{m}$. [Colour figure can be viewed at wileyonlinelibrary.com]

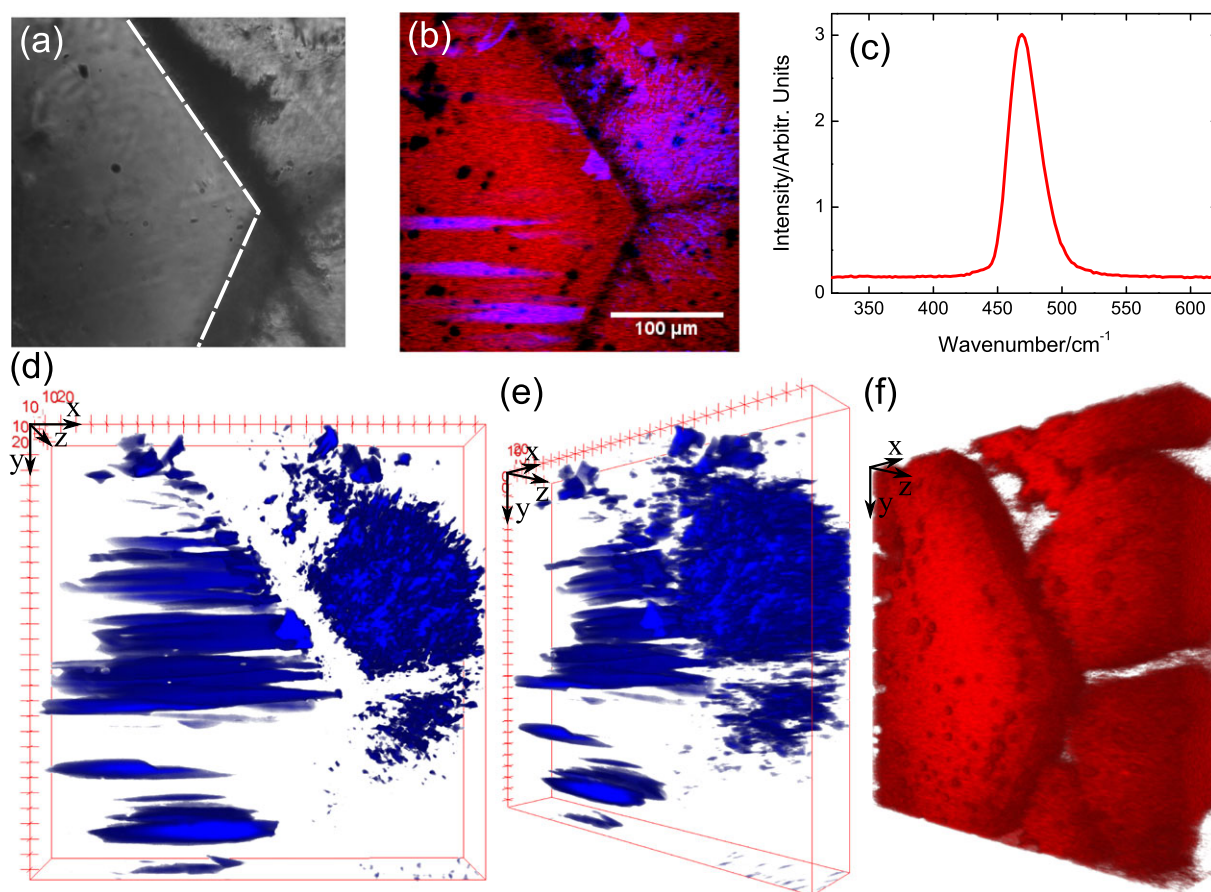


Figure 5. Sample M-K5A: (a) Bright-field transmitted-light microscopy image of a quartz sample. Dashed line marks the edge of a single crystal that is overgrown by fine-grained chalcedonic quartz. (b) Multimodal stimulated Raman scattering (SRS) (red) and second harmonic generation (blue) image. The scale bar is 100 μm . (c) SRS spectrum of quartz acquired with the spectral focusing technique of image (b). (d) Front and (e) orthogonal view of a 3D volume image of the second harmonic generation signal showing elongated planes of Brazil twins within the single crystal and grain boundaries of individual microcrystals within the chalcedony. (f) Orthogonal view of a 3D volume image of the SRS signal from quartz. [Colour figure can be viewed at wileyonlinelibrary.com]

chalcedonic quartz. The bright-field transmitted-light microscopy image of the ROI is shown in Fig. 5(a), and the quartz SRS spectrum acquired over the whole ROI is shown in Fig. 5(c). In Fig. 5(b), we show one image of the 3D volume acquired. While the SRS signal from quartz is present over the whole ROI, the SHG signal is generated only in specific areas. A 3D volume of the ROI [Fig. 5(d) and (e)] shows the different features created by the SHG signal. On the left side of the image, the SHG signal reveals elongated, parallel Brazil twinning, whereas on the right side of the image, the speckle-like structure of the SHG signal is due to different optical orientations of microcrystals within the chalcedony. These structures are not seen using SRS microscopy alone [Fig. 5(f)], as it only displays the volume occupied by quartz, chemically identified by its Raman spectrum but not its crystallinity.

In contrast with CARS microscopy, SRS is not affected by nonresonant four-wave mixing processes that can reduce sensitivity and distort the Raman spectrum. However, other types of nonresonant processes can affect SRS imaging. In principle, there are four possible sources of nonresonant background in SRS imaging: TL, XPM, ESA, and TPA.^[22] In Fig. 6, we show SRS images of sample B-1, a fossil foraminiferum cemented by calcite, which is affected by nonresonant signals. The pump laser wavelength was tuned to 934 nm to probe the calcite Raman peak at 1088 cm^{-1} . A bright-field transmitted-light microscopy image, Fig. 6(a), shows the ROI used for this analysis. In Fig. 6(b), we show an unprocessed SRS image

recorded at the 1088 cm^{-1} resonance Raman peak. It can be seen that there are bright regions which one might be tempted to assign uniquely to calcite, because of being on the 1088 cm^{-1} resonance. However, as we elaborate in the following, there are both resonant and nonresonant signals present in this image: these are not distinguishable via an intensity analysis alone. The chemical identification of the mineral calcite within the ROI can be only confirmed by scanning the SRS spectrum, as shown in Fig. 6(c) and (d). The ROIs used to produce the SRS spectra shown in Fig. 6(c) and (d) are displayed in Fig. 6(b). The SRS spectrum in Fig. 6(c) shows a sharp peak centered at 1088 cm^{-1} , confirming the presence of calcite. In contrast, the broad SRS spectrum of Fig. 6(d) reveals a predominantly nonresonant response which therefore cannot be due to calcite. The image brightness in this ROI must rather be due to TL, XPM, ESA, or TPA background effects. We can use the Raman spectral contrast to separate the nonresonant signals from the resonant SRS signals within the images. By detuning the probed Raman frequency by about 50 cm^{-1} , the resonant calcite SRS signal vanishes, whereas the nonresonant signal remains largely unchanged [Fig. 6(e)]. This image contrast obtains only from the nonresonant SRS response. Importantly, by subtracting the resonant SRS image (1088 cm^{-1}) from the nonresonant image (1040 cm^{-1}), we obtain directly the calcite-specific SRS image, shown in Fig. 6(f). In Fig. 6(g), we show the ROI with the calcite SRS resonant signal (green) and the nonresonant signal (gray)

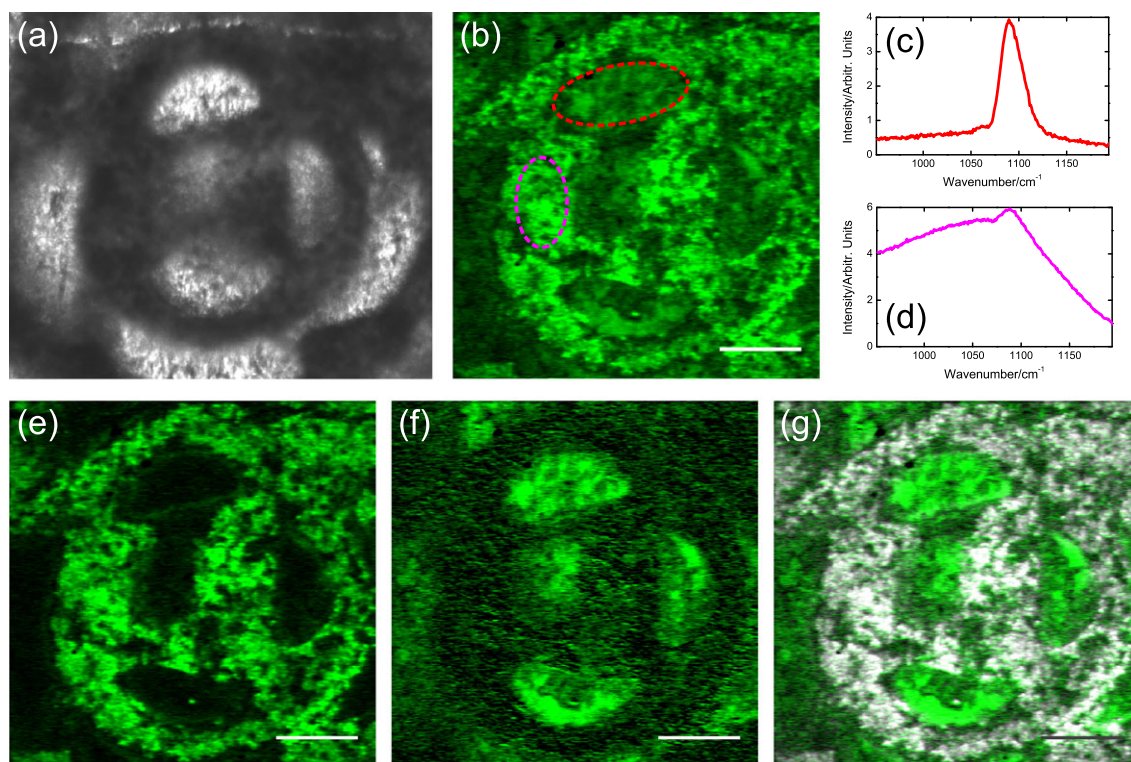


Figure 6. Sample B-1: (a) Bright-field transmitted-light image of a fossilized foraminifera within a calcite-rich sample. (b) Unprocessed stimulated Raman scattering (SRS) image of calcite showing the resonant signal from calcite as well as nonresonant signal. (c and d) SRS spectra of (c) calcite and (d) the nonresonant signal. The region of interest used to measure the SRS spectra are shown in (b) as the red (SRS) and magenta (nonresonant signal) circles. (e) SRS image with the frequency tuned at 1040 cm^{-1} (out of the calcite resonance peak) showing only the nonresonant signal. (f) Subtraction of image (b) and (e) showing only the resonant SRS signal from calcite. (g) Composite image of (e) and (f) showing the resonant SRS signal from calcite (green) as well as the nonresonant signal (gray). For a better visualization of the images, the brightness of the SRS signal for (f) and (g) was increased by a factor 2. The scale bars are $50\text{ }\mu\text{m}$. [Colour figure can be viewed at wileyonlinelibrary.com]

displayed, highlighting the different features within the sample. Importantly, this study demonstrates the critical importance of rapidly scanning the Raman spectral lineshape to confirm the chemical or mineralogical identity of the species under question: image intensity alone generally will not suffice to identify the chemical nature of the species. Single-spectral-point imaging (i.e. a single, fixed SRS Raman shift) would have failed dramatically in identifying the spatial distribution of calcite within this sample.

Spectrally resolved SRS microscopy is also important for distinguishing minerals having close-lying Raman bands. In Fig. 7, we show an SRS image of sample B-2 that contains small anhydrite crystals embedded within a calcite crystal. In Fig. 7(a), we show a bright-field transmitted-light microscopy image of the ROI used for this analysis. Because anhydrite and calcite have Raman peaks within 100 cm^{-1} of each other, we can very rapidly scan the Raman spectrum using our spectral focusing method. By centering the pump laser wavelength at 937 nm , both Raman peaks (calcite at 1088 cm^{-1} , anhydrite at 1017 cm^{-1}) can be probed by rapidly scanning the pump-Stokes time delay (i.e. the spectral focusing method). In Fig. 7(b), we show an SRS image with the resonant calcite signal in green and the anhydrite resonant signal in cyan. The recorded SRS spectra of these minerals are shown in Fig. 7(c), with the relevant ROIs being shown in Fig. 7(b). In Fig. 7(d), we show the maximum intensity projection of the 3D volume SRS signal, giving a better view of the shape of the anhydrite samples, whereas Fig. 7(e) shows the 3D volume of the ROI. Figure 7(d) shows in gray the signal from the 'out of phase' lock-in amplifier channel: this is a nonresonant signal due to TL. Because TL is generally (but not always) out

of phase with the SRS signal, the lock-in phase allows for enhanced signal separation.^[46] The TL signal is created by small absorbing particles that locally heat the sample. We note TL signals can appear in the SRS channel and be mistaken for small anhydrite crystals. Again, spectral scanning unambiguously identifies the mineral. A 3D volume image of the anhydrite distribution is shown in Fig. 7(f), revealing 3D anhydrite crystal shape and its boundaries.

At this point in the discussion, a comparison between the acquisition time between SRS microscopy and conventional Raman microscopy should be addressed. The imaging speed of Raman microscopy usually ranges between tens of minutes to hours to attain a resolved image. A current state-of-the-art conventional Raman microscope^[39] requires hours to acquire a 256×256 pixels image with a pixel dwell time of a few tens of millisecond. Such an acquired image has the advantage of containing a complete Raman spectrum at each pixel. However, SRS microscopy offers the possibility of (i) acquiring images while changing the time delay between the pump and the Stokes to obtain a Raman spectrum (hyperspectral imaging) or (ii) acquiring images, very rapidly, at a fixed Raman shift. Hence, at a specific Raman shift, it is possible to acquire an image in a matter of seconds or a 3D volume in a matter of minutes (Table 1), with a pixel dwell time three orders of magnitude faster than conventional Raman microscopy. Furthermore, with the spectral focusing technique, it is possible to quickly scan the Raman lineshape of an image over a limited range (here, approximately 150 cm^{-1}). This can be performed in a time scale ranging between 5 and 10 min per image, depending of the required spectral range and resolution. To acquire the whole Raman

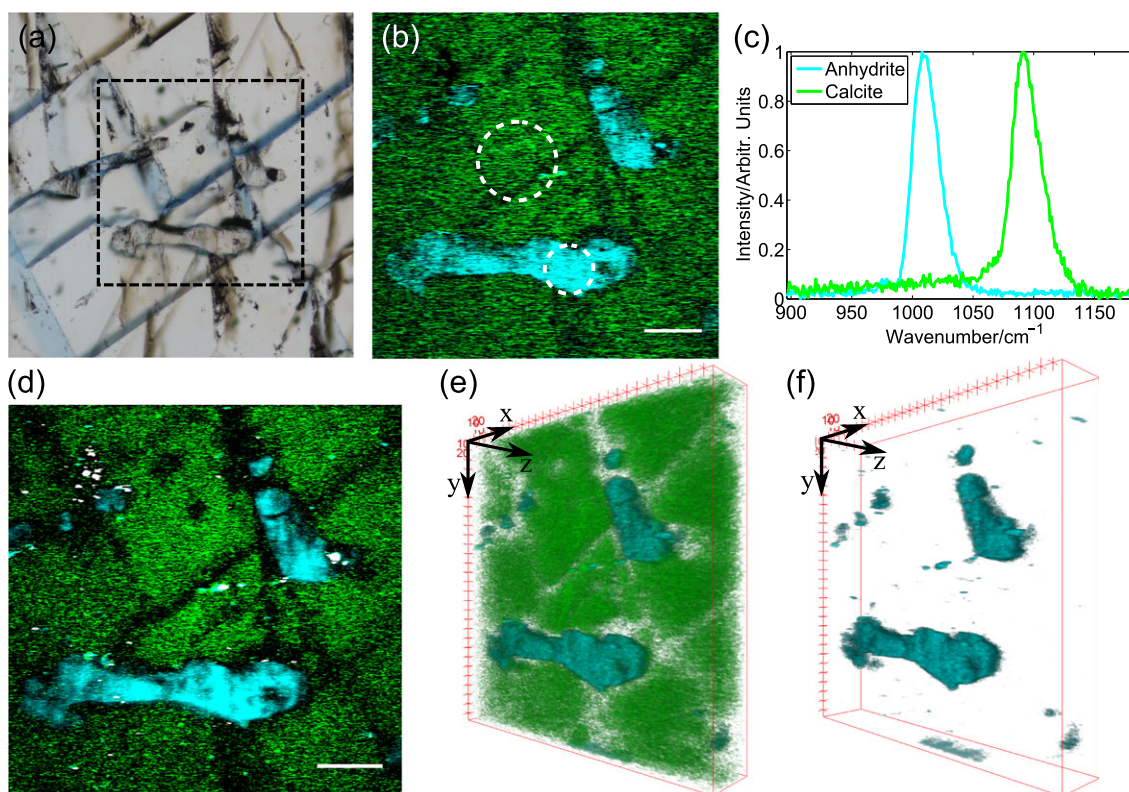


Figure 7. Sample B-2 of isolated anhydrite crystals embedded in a large calcite crystal: (a) Bright-field transmitted-light image of the sample. The square represents the region of interest imaged with the stimulated Raman scattering (SRS) microscope. (b) SRS image of the sample where the calcite is shown in green, and anhydrite is shown in cyan. The pump wavelength was tuned to 937 nm, and the frequency was tuned to 1088 cm^{-1} to acquire the calcite signal and 1017 cm^{-1} to acquire the anhydrite signal. The scale bar is 50 μm . (c) SRS spectrum of the regions of interest shown in (b). Both spectra were acquired during a single SRS scan. For a better visualization, the spectra are normalized so that they have the same intensity. (d) SRS image of the maximum intensity projection of the volume acquisition. In gray is the signal from the Y channel from the lock-in amplifier that represents the nonresonant signal due to thermal lensing. (e) Orthogonal view of the 3D volume image of the SRS signal from calcite and anhydrite. (f) Orthogonal view of the 3D volume image of the SRS signal from anhydrite. [Colour figure can be viewed at wileyonlinelibrary.com]

spectrum, multiple rapid spectral scans need to be acquired and stitched together, which yields an overall hyperspectral imaging speed closer to that of conventional Raman microscopy. However, as previously mentioned, in the cases where only a small frequency range need to be probed or a specific Raman frequency (i.e. a specific mineral) need to be imaged, SRS microscopy is much faster. Finally, SRS can be naturally combined with other nonlinear imaging modalities such as SHG or two-photon excitation fluorescence.

Conclusion

We have demonstrated the first application of multimodal SRS microscopy to the earth sciences, specifically the imaging of minerals and fluid inclusions. Unlike Raman microscopy, SRS microscopy can produce chemically specific high 3D-resolution images in seconds, even in the presence of sample fluorescence. Spectral focusing allows rapid scanning of the Raman spectral lineshape over a range of approximately 150 cm^{-1} without tuning the laser output, demonstrated here for the imaging of minerals having closely spaced Raman bands (e.g. calcite and anhydrite). The overall Raman-tuning range of our setup is 400–4500 cm^{-1} . SRS microscopy can also be easily combined with SHG microscopy to provide additional information on the structure of non-centrosymmetric minerals. However, nonresonant background signals can appear in SRS microscopy. For example, we showed in sample B-1 (fossil

foraminifera and Fig. 6) that image intensity can originate from other nonlinear processes. We therefore emphasize that scanning the SRS spectrum over the Raman lineshape is required to confirm the true chemical nature of the species under investigation. Background signals due to TL, XPM, ESA, and TPA can contribute to image intensity in SRS but do not exhibit a Raman resonance. Single-spectral-point imaging, which relies on image intensity alone, may not be able to distinguish the resonant Raman response from these background signals. Although our current setup is laser bandwidth limited to a 'rapid tuning range' of approximately 150 cm^{-1} , we are currently working on fiber-based nonlinear propagation methods for increasing the bandwidth of the Stokes pulse to achieve a larger spectral range within a rapid single scan. Finally, SRS microscopy can also be applied to the imaging of trapped higher organic matter (e.g. crude oil) in geologic samples. This will be presented in another publication. We anticipate that SRS microscopy will find use in the Earth Sciences, particularly in the mineralogy, petroleum, and mining research communities.

Acknowledgements

The authors acknowledge the financial support of the Natural Sciences and Engineering Research Council of Canada (NSERC) and the Innovation Center for Earth Sciences of the US Geological Survey. Any use of trade, firm, or product names is for descriptive

purposes only and does not imply endorsement by the US Government.

References

- [1] W. D. Carlson, *Earth Planet. Sci. Lett.* **2006**, *249*, 133.
- [2] G. Nehrke, J. Nouet, *Biogeosciences* **2011**, *8*, 3761.
- [3] J. W. Schopf, A. B. Kudryavtsev, V. N. Sergeev, *J. Paleo.* **2010**, *84*, 402.
- [4] L. Nasdala, O. Beyssac, J. W. Schopf, B. Bleisteiner, in *Raman Imaging* (Ed: A. Zoubir), Springer, Berlin Heidelberg, **2012**, pp. 145.
- [5] M. Fries, A. Steele, in *Confocal Raman Microscopy* (Eds: T. Dieing, O. Hollricher, J. Toporski), Springer, Berlin Heidelberg, **2010**, pp. 111.
- [6] A. Wang, R. L. Korotev, B. L. Jolliff, Z. Ling, *Planet. Space Sci.* **2015**, *112*, 23.
- [7] M. Andreana, A. Stolow, *Opt. Photonics News* **2014**, *25*, 43.
- [8] A. Zumbusch, G. R. Holtom, X. S. Xie, *Phys. Rev. Lett.* **1999**, *82*, 4142.
- [9] E. O. Potma, X. S. Xie, *Opt. Photonics News* **2004**, *15*, 40.
- [10] C. L. Evans, X. S. Xie, *Annu. Rev. Anal. Chem.* **2008**, *1*, 883.
- [11] J. Cheng, A. Volkmer, L. D. Book, X. S. Xie, *J. Phys. Chem. B* **2001**, *105*, 1277.
- [12] M. D. Duncan, J. Reintjes, T. J. Manuccia, *Opt. Lett.* **1982**, *7*, 350.
- [13] J.-X. Cheng, A. Volkmer, X. S. Xie, *J. Opt. Soc. Am. B* **2002**, *19*, 1363.
- [14] P. Nandakumar, A. Kovalev, A. Volkmer, *New J. Phys.* **2009**, *11*, 033026.
- [15] C. W. Freudiger, W. Min, B. G. Saar, S. Lu, G. R. Holtom, C. He, J. C. Tsai, J. X. Kang, X. S. Xie, *Science* **2008**, *322*, 1857.
- [16] F. Gao, F. Shuang, J. Shi, H. Rabitz, H. Wang, J.-X. Cheng, *J. Chem. Phys.* **2012**, *136*, 144114.
- [17] F. Ganikhanov, C. L. Evans, B. G. Saar, X. S. Xie, *Opt. Lett.* **2006**, *31*, 1872.
- [18] K. I. Popov, A. F. Pegoraro, A. Stolow, L. Ramunno, *Opt. Express* **2011**, *19*, 5902.
- [19] A. M. Barlow, K. Popov, M. Andreana, D. J. Moffatt, A. Ridsdale, A. D. Slepko, J. L. Harden, L. Ramunno, A. Stolow, *Opt. Express* **2013**, *21*, 15298.
- [20] K. I. Popov, A. F. Pegoraro, A. Stolow, L. Ramunno, *Opt. Lett.* **2012**, *37*, 473.
- [21] H. A. Rinia, M. Bonn, M. Müller, *J. Phys. Chem. B* **2006**, *110*, 4472.
- [22] P. Berto, E. R. Andresen, H. Rigneault, *Phys. Rev. Lett.* **2014**, *112*, 053905.
- [23] D. Fu, T. Ye, T. E. Matthews, B. J. Chen, G. Yurtserver, W. S. Warren, *Opt. Lett.* **2007**, *32*, 2641.
- [24] M. C. Fischer, J. W. Wilson, F. E. Robles, W. S. Warren, *Rev. Sci. Instrum.* **2016**, *87*, 031101.
- [25] K. Ekvall, P. van der Meulen, C. Dhollande, L.-E. Berg, S. Pommeret, R. Naskrecki, J.-C. Mialocq, *J. Appl. Phys.* **2000**, *87*, 2340.
- [26] K. Uchiyama, A. Hibara, H. Kimura, T. Sawada, T. Kitamori, *Jpn. J. Appl. Phys., Part 1* **2000**, *39*, 5316.
- [27] D. Zhang, M. N. Slipchenko, J.-X. Cheng, *J. Phys. Chem. Lett.* **2011**, *2*, 1248.
- [28] M. Andreana, M.-A. Houle, D. J. Moffatt, A. Ridsdale, E. Buettner, F. Légaré, A. Stolow, *Opt. Express* **2015**, *23*, 28119.
- [29] J. L. Suhalim, J. C. Boik, B. J. Tromberg, E. O. Potma, *J. Biophotonics* **2012**, *5*, 387.
- [30] C. H. Camp Jr., M. T. Cicerone, *Nat. Photonics* **2015**, *9*, 295.
- [31] C. Zhang, D. Zhang, J.-X. Cheng, *Annu. Rev. Biomed. Eng.* **2015**, *17*, 415.
- [32] A. F. Pegoraro, A. D. Slepko, A. Ridsdale, D. J. Moffatt, A. Stolow, *J. Biophotonics* **2014**, *7*, 49.
- [33] C. H. Camp Jr., Y. J. Lee, J. M. Heddleston, C. M. Hartshorn, A. R. H. Walker, J. N. Rich, J. D. Lathia, M. T. Cicerone, *Nat. Photonics* **2014**, *8*, 627.
- [34] B.-C. Chen, J. Sung, S.-H. Lim, *J. Phys. Chem. B* **2010**, *114*, 16871.
- [35] B.-C. Chen, J. Sung, X. Wu, S.-H. Lim, *J. Biomed. Opt.* **2011**, *16*, 021112.
- [36] N. Dudovich, D. Oron, Y. Silberberg, *J. Chem. Phys.* **2003**, *118*, 9208.
- [37] D. Fu, F.-K. Lu, X. Zhang, C. Freudiger, D. R. Pernik, G. Holtom, X. S. Xie, *J. Am. Chem. Soc.* **2012**, *134*, 3623.
- [38] R. C. Burruss, A. D. Slepko, A. F. Pegoraro, A. Stolow, *Geology* **2012**, *40*, 1063.
- [39] A. V. Korsakov, J. Toporski, T. Dieing, J. Yang, P. S. Zelenovskiy, *J. Raman Spectrosc.* **2015**, *46*, 880.
- [40] A. F. Pegoraro, A. Ridsdale, D. J. Moffatt, Y. Jia, J. P. Pezacki, A. Stolow, *Opt. Express* **2009**, *17*, 2984.
- [41] T. A. Pologruto, B. L. Sabatini, K. Svoboda, *Biomed. Eng. Online* **2003**, *2*, 13.
- [42] J. Schindelin, I. Arganda-Carreras, E. Frise, V. Kaynig, M. Longair, T. Pietzsch, S. Preibisch, C. Rueden, S. Saalfeld, B. Schmid, J.-Y. Tinevez, D. J. White, V. Hartenstein, K. Eliceiri, P. Tomancak, A. Cardona, *Nat. Methods* **2012**, *9*, 676.
- [43] E. Roedder, in *Fluid Inclusions: Reviews in Mineralogy* (Ed: P. H. Ribbe), Mineralogical Society of America, Washington, **1984**.
- [44] B. Schrader, W. Meier, *Raman/IR Atlas of Organic Compounds*, Wiley-VCH Verlag GmbH, Weinheim, **1976**.
- [45] P. Stoller, P. M. Celliers, K. M. Reiser, A. M. Rubenchik, *Appl. Optics* **2003**, *42*, 5209.
- [46] J. Moger, N. L. Garrett, D. Begley, L. Mihoreanu, A. Lalatsa, M. V. Lozano, M. Mazza, A. Schatzlein, I. Uchegbu, *J. Raman Spectrosc.* **2012**, *43*, 668.